INLAND WATERS
https://doi.org/10.1080/20442041.2018.1533356

Under-ice convection dynamics in a boreal lake

Damien Bouffard [a], Galina Zdorovennova [b], Sergey Bogdanov [b], Tatyana Efremova [b], Sébastien Lavanchy [c], Nikolay Palshin [b], Arkady Terzhevik [b], Love Råman Vinnå [a], Sergey Volkov [b], Alfred Wüest [a,c], Roman Zdorovennov [b] and Hugo N. Ulloa [c]

[a]Eawag, Swiss Federal Institute of Aquatic Science and Technology, Surface Waters – Research and Management, Kastanienbaum, Switzerland; [b]Northern Water Problems Institute, Karelian Research Centre, Russian Academy of Sciences, Petrozavodsk, Russia; [c]Physics of Aquatic Systems Laboratory, Margaretha Kamprad Chair, École Polytechnique Fédérale de Lausanne, Institute of Environmental Engineering, Lausanne, Switzerland

ABSTRACT

We investigated radiatively driven under-ice convection in Lake Onego (Russia) during 3 consecutive late winters. In ice-covered lakes, where the temperature of water is below the temperature of maximum density, radiatively driven heating in the upper water column induces unstable density distributions leading to gravitational convection. In this work, we quantified the key parameters to characterise the radiatively driven under-ice convection: (1) the effective buoyancy flux, B_* (driver), and its vertical distribution; (2) the convective mixed-layer thickness, h_{CML} (depth scale); and (3) the convective velocity, w_*(kinematic scale). We compared analytical w_* scaling estimates to in situ observations from high-resolution acoustic Doppler current profilers. The results show a robust correlation between w_* and the direct observations, except during the onset and decay of the solar radiation. Our results highlight the importance of accurately defining the upper limit of h_{CML} in highly turbid water and the need for spectrally resolving solar radiation measurements and their attenuation for accurate B_* estimates. Uncertainties in the different parameters were also investigated. We finally examined the implications of under-ice convection for the growth rate of nonmotile phytoplankton and provide a simple heuristic model as a function of easily measurable parameters.

ARTICLE HISTORY
Received 5 March 2018
Accepted 2 October 2018

KEYWORDS
phytoplankton growth; radiatively driven convection; under-ice measurements; winter limnology

Introduction

Ice-covered lakes are largely disconnected from external kinetic and thermal atmospheric energy (Kirillin et al. 2012). Late winter has long been assumed as a quiescent period for inland waters before spring melt and water reset the thermal and biogeochemical conditions of the ice-free period. Yet, ice-covered lakes remain complex, hosting active biogeochemical processes (Powers and Hampton 2016, Hampton et al. 2017). The disconnection from the atmosphere and cessation of the air–water gas exchanges can lead to anoxic conditions (Golosov et al. 2007). Similarly, the under-ice lake carbon dynamics result in an accumulation and a late CO_2 evasion estimated to significantly contribute to the annual CO_2 flux (Ducharme-Riel et al. 2015). Lastly, algal growth is observed in various ice-covered lakes despite the low light and low temperature conditions (Twiss et al. 2014), as for instance in Lake Baikal where under-ice diatom blooms can account for a large part of the annual production (Katz et al. 2015). A growing number of observations have undermined the traditional quiescent representation of under-ice limnology (Powers and Hampton 2016), and the coupling between physical and biogeochemical processes should be further investigated.

In the global context of climate change, the phenology of lake ice is of primary importance because the timing of freezing and thawing might strongly affect the lacustrine processes, yet the role of the physical processes in winter limnology remains substantially overlooked. At the end of winter, the intensity of solar radiation can become strong enough to penetrate the ice. One direct implication is the availability of energy for photosynthesis. With water cooler than the temperature of maximum density (T_{MD} = 3.984 °C for zero salinity), solar radiation increases the near-surface water density and leads to gravitational convective instabilities (Bouffard and Wüest 2019). Thus, heating by radiative energy modifies the vertical temperature profile of the lake by setting up a convective mixed layer (CML).

CONTACT Damien Bouffard damien.bouffard@eawag.ch

Radiatively driven convection has been observed in late winter in ice-covered lakes (Farmer 1975, Bengtsson 1996, Mironov et al. 2002, Jonas et al. 2003, Forrest et al. 2008, Kirillin et al. 2015, Bouffard et al. 2016) with subsequent local- to basin-scale circulation. In addition to the direct effect of solar radiation to trigger photosynthetic activity, radiatively driven convection can redistribute deeper nutrients and increase the retention time of phytoplankton in the photic surface layer (Pernica et al. 2017). The nonmotile phytoplankton growth under the ice is an interesting example of a coupled biophysical process. Solar radiation is both the trigger for growth as well as the curator for the environmental niche via the development of a convective layer with thermal plumes counteracting the settling of phytoplankton.

Kelley (1997) compared the sinking rate of nonmotile phytoplankton with the updraft convective velocity, which depends on the buoyancy flux and the thickness of the CML, h_{CML}. A scaling for the convective velocity was established from laboratory experiments (Deardorff 1970) and was extended in the case of volumetric radiative forcing of under-ice convection (Mironov et al. 2002). This scaling predicts under-ice convective velocity that typically ranges from 1 to 7 mm s^{-1} in lakes (Farmer 1975, Bouffard et al. 2016). Yet to date there is no direct estimate of the vertical velocity in the radiatively driven under-ice convective layer. Previous velocity estimations have focused on horizontal currents due to seiches (Malm et al. 1998) and more recently on gyres (Forrest et al. 2013) and downslope density currents (Kirillin et al. 2015). The challenge in the Deardorff scaling is to relate the strength of the convection to the incoming solar radiation and optical properties of the water. Indeed, the parameterization of the transfer of solar energy is complex. First, parts of the incoming solar radiation are reflected by snow and ice at the surface. Other parts are absorbed by the ice, depending on its properties (Leppäranta et al. 2003, Zdorovennova et al. 2013a). Finally, the remainder of solar radiation is absorbed throughout the water column, and its vertical distribution depends on the quantity of particles. Yet, the absorption is not uniform over the wavelength, and the light spectrum is not only modified in intensity but also in shape. This phenomenon is particularly relevant for waters with high coloured dissolved organic matter (CDOM), such as Lake Onego bay (Sabylina and Ryzhakov 2018), where the short wavelength radiation is strongly absorbed compared to the rest of the visible spectra (Röttgers and Doerffer 2007). With the recent development of underwater hyperspectral radiometers, the wavelength-dependent penetration and absorption of the visible domain relevant for the heat budget can be assessed.

The goal of this study was to evaluate the scaling parameterization of the radiatively driven convection under ice by direct observations of the convection. Specifically, we evaluated (1) the role of the vertical and spectral distribution of the incoming radiative energy and (2) the uncertainties of the relevant physical parameters. Finally, we illustrated how these parameters can be used in ecological studies to assess whether or not convection can favour nonmotile phytoplankton growth.

Methods and data

Radiatively driven under-ice convection was investigated over 3 successive late winter periods in March (2015, 2016, and 2017) in Lake Onego (also called Lake Onega), Russia. Measurements were performed 2 km from the shore in Petrozavodsk Bay at 61°46,744′N, 34° 25,793′E, where the water column was 27 m deep (Fig. 1).

Thermal structure of the water column

The thermal structure of the water column was monitored with RBR temperature sensors mounted with vertical spacing increasing with depth (see Appendix A for setting and characteristics of all instruments and Fig. 1 for setup). For 2016 and 2017, an additional mooring was deployed with 10 high-resolution, fast-responding RBR temperature sensors with 2.5 cm vertical spacing from the ice–water interface to 0.25 m below it. This fine-scale resolution of the temperature directly below the ice provided information on the dynamics of the under-ice diffusive layer (UIDL) and an accurate estimate of the upper boundary of the CML at $z = -\delta$ (m). The spatially discretized observation of the thermal structure was complemented by hourly conductivity, temperature, and depth (CTD) profiles resolving precisely and continuously the lower bound $z = -h_M$ of the CML. The vertical extent of the CML was determined by $h_{CML} = h_M - \delta$ (m). Two conductivity loggers were moored in the CML in 2017, showing low and constant salinity over the measuring period (27 [SD 0.7] μS cm^{-1}). Salinity and salt exclusion during the freezing/thawing process can modify the local density structure under the ice (Bluteau et al. 2017), yet the observed low conductivity and almost constant ice thickness justified neglecting salinity effects in this study.

Temporal change of the mixed layer thickness

The increase in T_{CML} has a complex dependence on how the incoming radiative energy is vertically distributed.

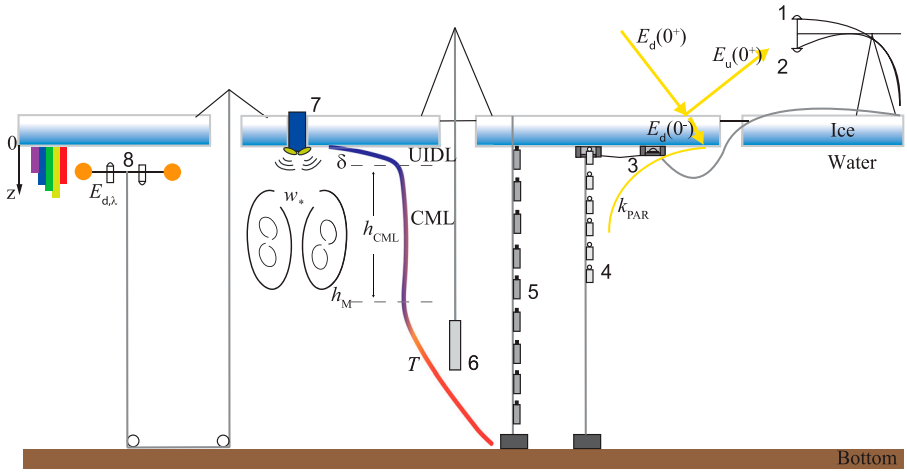

Figure 1. The experimental setup including pyranometers (1, 2, 3), PAR sensors (4), T-loggers (5), CTD-profiles (6), ADCPs (7), and hyperspectral radiometer profiles (8). Physical processes represented include light penetration transmittance (yellow arrows) and albedo (yellow curve), spectrally resolved light distribution (rainbow spectra), and temperature profile and convective cells. The different layers (under-ice diffusive layer [UIDL] and convective mixed layer [CML]) and their thicknesses (δ and h_CML, respectively) are indicated.

Briefly, part of the incoming energy directly goes into background potential energy (e.g., warming of the layer) while another part is transformed into available potential energy. This energy component is then converted into kinetic energy (e.g., convective plumes) that in turn enhances mixing, consequently deepening the h_{CML}. However, part of the kinetic energy is expended impinging the lower bound of the CML, a process that transfers energy from the convective cells to the internal wavefield in the deep stratified layer, while the rest of the kinetic energy is irreversibly dissipated by friction. This chain of energy conversions leads to an increase in the background potential energy of the system. A detailed analysis of the energy pathway in radiatively heated ice-covered lakes was provided by Ulloa et al. (2018).

The deepening of h_{CML} can be approximated by (Zilitinkevich 1991, Kirillin et al. 2012):

$$\frac{dh_{CML}}{dt} = (1 + 2\xi)\frac{B_*}{h_{CML}N^2}, \quad (1)$$

with the entrainment coefficient ξ. Farmer (1975) estimated $\xi = 0.2$ for the ice-covered Lake Babine; B_* ($m^2 s^{-3} = W kg^{-1}$) is the buoyancy flux; and N^2 (s^{-2}) is the background stratification or water column stability just below the CML, defined as $N^2 = -\frac{g}{\rho}\frac{\partial \rho}{\partial z}$, with the gravitational acceleration g and the water density ρ.

Light penetration

The light penetration was measured with 3 pyranometers for downwelling irradiance above and below ice and upwelling irradiance above the ice (Fig. 1, Appendix A). This setup provided estimates of albedo and transmittance of the ice/snow layer (Leppäranta et al. 2010, Kirillin et al. 2012, Bouffard et al. 2016). Hereafter, we denote the downwelling and upwelling solar irradiance above the ice as $E_d(O^+)$ and $E_u(O^+)$, respectively, and the under-ice downwelling solar irradiance as $E_d(O^-)$, all in W m^{-2}. The albedo and transmittance are defined as $A = E_u(O^+)/E_d(O^+)$ and $T_r = E_d(O^-)/[(1 - A)E_d(O^+)]$, respectively. In this study, the most important parameter was $E_d(O^-)$, which represents the energy entering the water beneath the ice.

Nine photosynthetically active radiation (PAR) sensors were moored to measure the light as a function of depth and time and its attenuation based on Beer's law (1 m resolution for 2015/2016, ~0.3 m for 2017; see Appendix A). PAR (μmol m^{-2} s^{-1}) observations provided the integrated light spectrum (400–700 nm) at each depth and were used to estimate the light absorption, k_{PAR} (m^{-1}). Assuming that the solar radiation can be parameterized as a monochromatic source, downwelling solar irradiance decreases with depth by $E_d(z) = E_d(0^-)e^{-k_{PAR}z}$.

Moreover, the radiative spectral energy penetration of the sunlight was specifically investigated in 2016 with a setup similar to that used by Lei et al. (2011). A hyperspectral radiometer (Ramses VIS, Trios; Fig. 1) was deployed under the ice to record the downwelling irradiance at 190 wavelengths between $\lambda_1 = 320 < \lambda < 950 = \lambda_2$ nm (3.3 nm spectral resolution). We defined $E_{d,\lambda}(\lambda, z)$ (mW m^{-2} nm^{-1}), the spectrally resolved downwelling irradiance at depth z, and then the net downwelling irradiance by $\widetilde{E}_d(z) = \int_{\lambda_1}^{\lambda_2} E_{d,\lambda}(\lambda, z)d\lambda$. From the

hyperspectral radiometer profiles, we estimated the spectrally resolved light attenuation coefficient $k_\lambda(m^{-1})$ and the profile of downwelling solar irradiance as $\widetilde{E}_d(z) = \int_{\lambda_1}^{\lambda_2} E_{d,\lambda}(\lambda, 0^-)e^{-k_\lambda z}d\lambda$. The difference between $\widetilde{E}_d$ and E_d provides an estimate of the error made by modelling the solar radiation as a monochromatic source. Here, the depth dependencies of k_{PAR} and k_λ were not investigated, and we assumed homogeneous optical properties within the CML. Given the strong light absorption (discussed later), heterogeneities in k_{PAR} and k_λ in the deeper part of the CML did not affect our results. Finally, sunrise was defined as the time when the solar irradiation above ice exceeded 10 W m^{-2} (typically ~0730 h, local time). Note that astronomical noon is ~1350 h in the Petrozavodsk area for mid-March.

Parameterization of the convective velocity

The convective velocity $w_*(m\ s^{-1})$ was parameterized using the scaling relation for convective turbulence (Deardorff 1970), expanded for volumetric forcing (Mironov et al. 2002) and applied by Bouffard et al. (2016). Briefly, $w_*(m\ s^{-1})$ scales with the buoyancy flux, B_*, and h_{CML} by:

$$w_* = (h_{CML}B_*)^{1/3}. \quad (2)$$

B_* results from the absorption of solar radiation within h_{CML} and is given by (z is positive downward, $z = 0$ at the ice–water interface; Fig. 1):

$$B_* = \frac{1}{h_{CML}}\int_{h_{CML}} B(z)dz = -\frac{g}{\rho C_p h_{CML}}\int_{-h_M}^{-\delta} \alpha\frac{\partial H_Q(z)}{\partial z}(h_M + z)dz, \quad (3)$$

with ρ (kg m^{-3}) the density of the water in the CML, C_p (J K^{-1} kg^{-1}) the thermal capacity, and α the thermal expansion coefficient (K^{-1}, $\alpha < 0$). For under-ice processes, the heat flux, H_Q (W m^{-2}), can simply be expressed as $H_Q(z) = E_d(z)$. This form is similar to, yet more general than, the equation presented by Mironov et al (2002).

Direct estimate of the convective velocity

We measured vertical velocities, w(t), with one RDI 600 kHz Mode 11 ADCP and two HR 2 MHz Nortek Aquadopp, both downward-looking in pulse-to-pulse coherent mode. The ADCPs were kept frozen in the ice for the ~2 week duration of the field measurements in 2016 and 2017. No direct observations of the vertical velocities were made in 2015. The RDI and Aquadopp ADCPs ranged from 8.0 to 2.5 m under the ice, respectively. The convective velocity in the CML was estimated as:

$$w_*(t) = \left(\frac{1}{h_{CML}}\int_{-h_M}^{-\delta} w^2(t)dz\right)^{0.5}. \quad (4)$$

The time series of $w_*(t)$ was hourly averaged. Although the downward velocity over the entire CML could not be measured, an estimate of w_* based on high-resolution ADCP measurements was obtained from a layer of 1.0 m thickness in the upper region of the CML between 1 and 2 m depth. Although investigating the vertical velocity over the entire CML would be preferable, the CML thickness was larger than the ADCP vertical range, and the divergent-beam ADCP is not ideal for investigating narrow coherent structures such as convective plumes. We set the upper noise limit for the background vertical velocity to ~0.5 mm s^{-1} based on measurements at night.

Finally, the skewness of the ratio between upward ($w+$) and downward ($w-$) velocities provided an indication of the convective plumes structures. This ratio was calculated when the daytime-averaged upward travel distance closely matched the vertical downward distance (e.g., conservation of mass).

Results

We focused on the direct forcing (e.g., solar radiations) and change in thermal structure of the water column as the most important observable parameters to characterize under-ice convection. The temporal evolutions of air temperature as well as wind intensity and direction were reported (Appendix B).

Solar radiation and ice optical properties

The downwelling solar radiation $E_d(0^+)$ measured in March 2015, 2016, and 2017 (Fig. 2) indicates different weather scenarios depending on cloudiness (e.g., 23–24 March 2015, 11–16 March 2016, 13 and 17–19 March 2017). The maximum solar radiation was observed in 2015 and 2016 with $E_d(0^+)$ exceeding 750 W m^{-2}. Averaged solar radiations measured in 2017 were slightly weaker with 262 (SD 113) W m^{-2} (max: 697 W m^{-2}) compared to 2015 with 345 (135) W m^{-2} (max: 756 W m^{-2}), and 2016 with 351 (143) W m^{-2} (max: 753 W m^{-2}).

The upwelling solar radiation $E_u(0^+)$ (Fig. 2) was also much larger in 2016, when midday (1100–1500 h) albedo was ~0.71 (SD 0.05) and nearly constant over the 12 d period (Fig. 3b). This measurement was

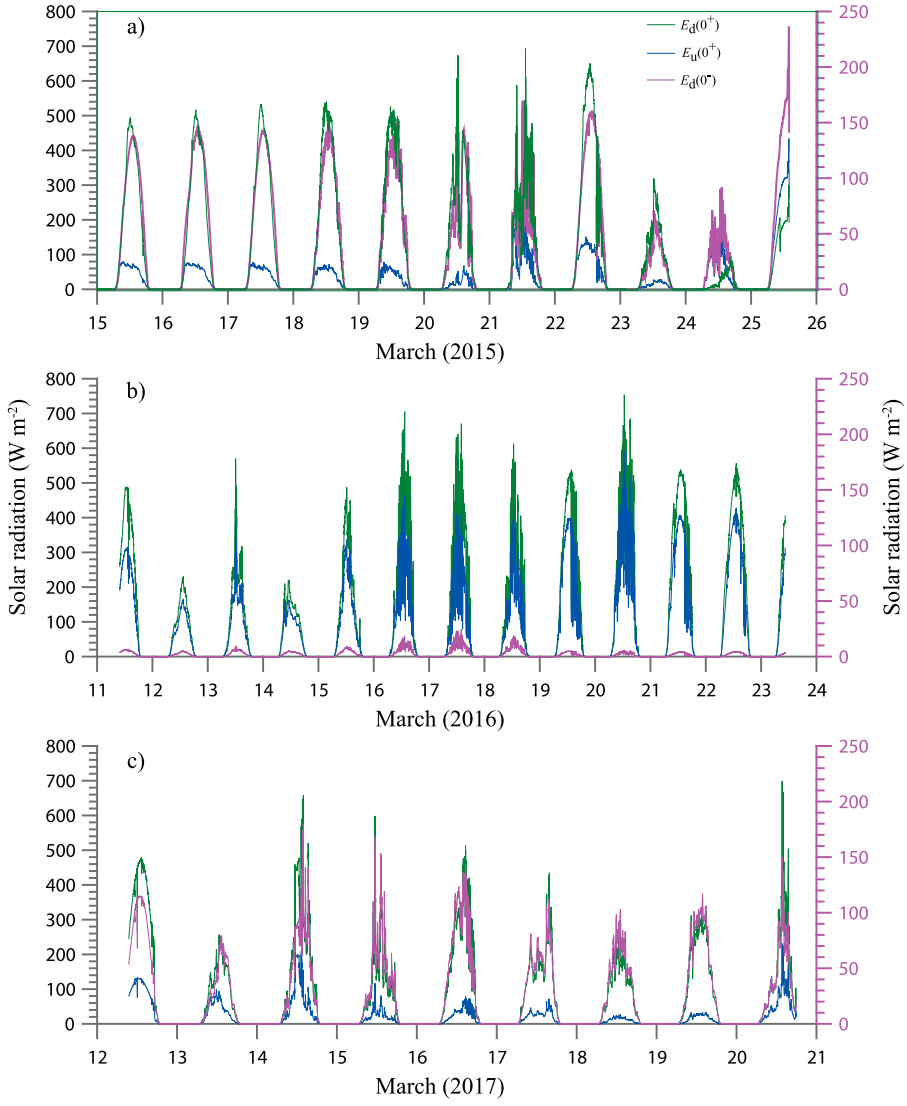

Figure 2. Downwelling irradiance $E_d(0^+)$ above the ice (green), upwelling irradiance $E_u(0^+)$ above the ice (blue), and downwelling irradiance $E_d(0^-)$ below the ice (purple) for (a) 2015, (b) 2016, and (c) 2017. Note that $E_d(0^-)$ is shown on the right axis on a finer range.

consistent with the observations of a thin patchy layer (up to 5 cm) of snow above the ice surface. Despite the large $E_d(0^+)$ in 2016, most of the light was reflected by ice and snow, and the measured $E_d(0^-)$ of 6 (SD 3) W m^{-2} was drastically lower than for the other years: 108 (50) W m^{-2} in 2015 and 79 (25) W m^{-2} in 2017.

For 2015, the average midday albedo was 0.23 (SD 0.18; Fig. 3a). The large standard deviation was due to strong weather variability during the field campaign. There was no snow on the ice, and the average midday albedo was ~0.15 and ~0.33 during the first and second half of the observed period, respectively. In 2016 the albedo reached a midday average value of 0.71 (SD 0.05; Fig. 3b), and in 2017 the average midday albedo was 0.21 (SD 0.10; Fig. 3c). All 3 periods in March revealed a daily pattern in the albedo with a decrease in the afternoon due to ice melting.

The transmittance (Fig. 3) was also different for the 3 late winters, with a midday average value of $Tr = 0.42$ (SD 0.14) in 2015, 0.07 (0.05) in 2016, and 0.40 (0.05) in 2017, indicating that between ~60% and ~90% of the solar radiation was absorbed by the ice. Black ice and white ice thicknesses were 39 and 0 cm in 2015, 40 and 9 cm in 2016, and 43 and 3 cm in 2017, respectively.

Despite the high incoming solar radiation in 2016, the thin layer of snow above the 9 cm of white ice reflected and absorbed (Petrov et al. 2005) most of the light and resulted in lower solar radiation penetrating the water. In conclusion, in 2015 and 2016 we observed similar incoming solar radiation during the measuring periods. Yet, the ice and snow properties were different, and ice optical properties and penetrative solar radiation were more similar in 2015 and 2017.

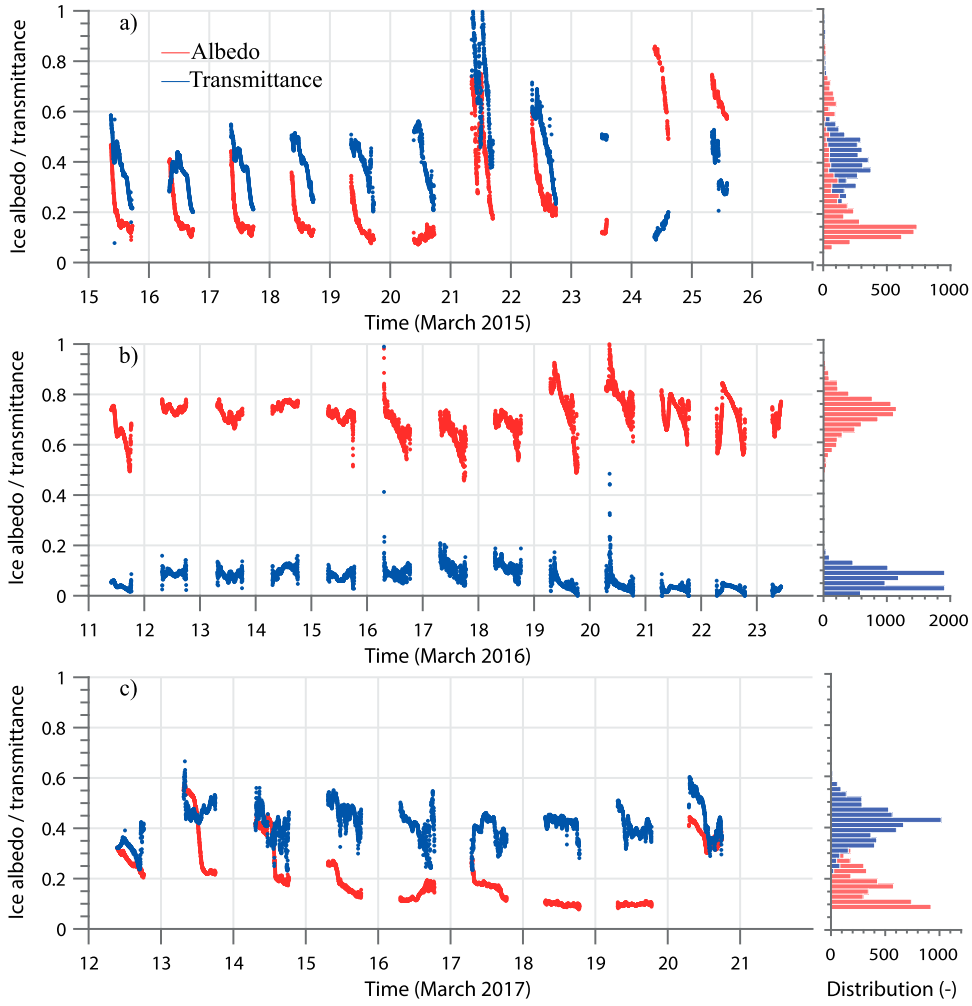

Figure 3. Ice albedo (red) and transmittance (blue) for (a) 2015, (b) 2016, and (c) 2017. Note the difference in albedo and transmittance between measurements in 2015/2017 and 2016. The histograms are shown on the right panel.

Light absorption

Despite the largest solar radiation $E_d(0^+)$ observed in March 2016, the weakest light intensity $E_d(0^-)$ was measured for this period below the ice (Fig. 2). This observation is consistent with the under-ice light measurements (Fig. 4), in which the solar radiation across the water column was one order of magnitude smaller in 2016 than in 2015 and 2017. Light penetrated to ~4 m depth (PAR $\geq$ 1 µmol m^{-2} s^{-1}) in March 2015 (Fig. 3a), ~1.5 m in 2016 (Fig. 3b), and ~2.5 m in 2017 (Fig. 3c). The PAR attenuation coefficient in the depth range of 1–2 m was k_{PAR} = 1.2 (SD 0.3) m^{-1} for March 2015, k_{PAR} = 3.2 (0.5) m^{-1} for 2016, and k_{PAR} = 2.7 (0.1) m^{-1} for 2017, corresponding to overall turbid water conditions. Visual inspection of collected samples indicated yellowish waters as typically observed in coloured dissolved organic matter (CDOM) dominated lakes. Indeed, the large absorption in the short wavelengths, typically responsible for this colour, is a signature of CDOM (Röttgers and Doerffer 2007), which was clearly shown with underwater hyperspectral measurements (Fig. 5). Although the mean k_λ across the range of 400 $<$ λ $<$ 700 nm was 2.6 m^{-1}, the attenuation coefficient varied from 1.2 m^{-1} at λ = 700 nm (higher wavelength are contaminated by sensor accuracy) to 5 m^{-1} at λ = 450 nm. Given the large absorption at small wavelengths (Fig. 5a), only the largest wavelengths (600 $<$ λ $<$ 700 nm) still contain energy below 1 m depth (Fig. 5b). The spectral distribution of energy differs from the monochromatic assumption made when using PAR and pyranometer sensors.

Thermal structure

The thermal structure of the water column had the same pattern for all 3 late winters (Fig. 6), with a top under-ice diffusive layer (UIDL), followed by the CML, and ending with a near bottom stratified layer. Yet the evolution of the CTD profiles showed different dynamics (Fig. 6).

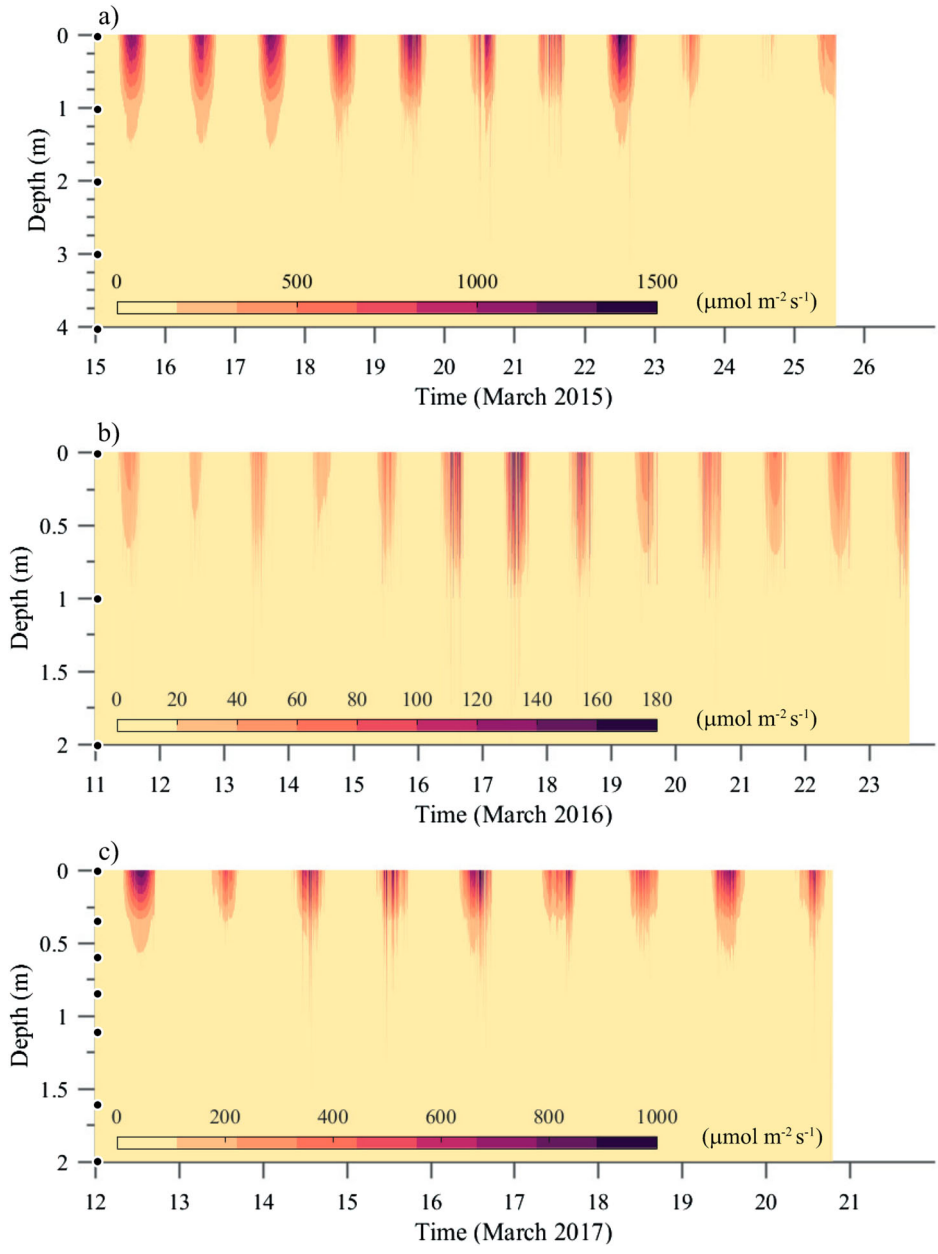

Figure 4. Vertically resolved light penetration measured with PAR sensors for (a) 2015, (b) 2016, and (c) 2017. Black dots indicate the depth of the PAR sensors. Note the large difference in energy penetrating into the convective mixed layer (CML) between 2016 and 2015/2017.

In 2015, we first observed a warming phase followed by restratification (after 21 March) of the previous CML. In 2016, the temperature profiles did not change significantly over time. In contrast with the previous years, we observed both a consistent warming and deepening of the CML in 2017. We described the daytime vertical thermal structure starting from the top.

The UIDL immediately below the ice was characterized by a steep, thin temperature gradient between the ice and the CML. The UIDL exhibited a clear diurnal variability (Fig. 7b). The night-averaged UIDL profile was a diffusive thermal layer subject to the ice-temperature boundary condition, $T_{ice} = 0$ °C, and a lower limit temperature, T_{CML}, set in the upper CML at the end of the day before. The day-averaged UIDL was characterized by a much steeper stable thin diffusive layer that separated the ice from the maximum temperature and was followed by an unstable ~10 to ~20 cm thick layer below (blue line in Fig. 7a). Above the maximum temperature, the incoming radiation was stabilizing the layer while below the T_{MD} the incoming radiation contributed to drive convection. Below, the vertical temperature gradient flattened, defining the classical CML (Fig. 7a). This diurnal UIDL structure can be

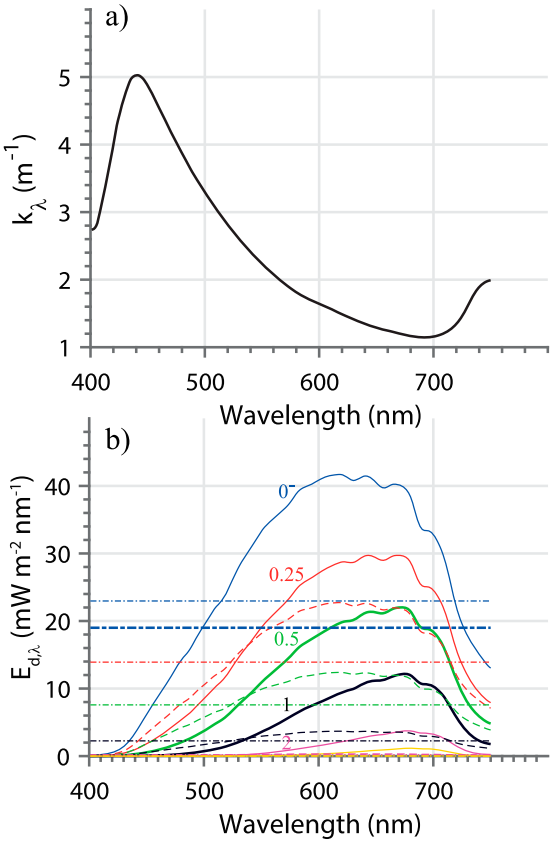

Figure 5. (a) Light attenuation as a function of wavelength between 0.5 and 1 m below the surface on 16 March 2016, 1200 h local time (e.g., midday). (b) Spectrally resolved downwelling irradiance, $E_{d,\lambda}(\lambda, z)$ measured at 0.5 m and 1 m (thick green and black lines). Thin lines are calculated from $E_{d,\lambda}(\lambda, z)$ based on spectrally resolved light attenuation coefficient k_λ (a). Dashed lines represent the vertical evolution of $E_{d,\lambda}(\lambda, z)$ based on spectrally averaged light attenuation coefficient (e.g., equivalent to k_{PAR} estimated from PAR measurements). Horizontal light dash-dotted lines represent the vertical evolution of spectrally averaged $\frac{1}{720-420}\int_{420}^{720} E_{d,\lambda}(\lambda, z)d\lambda$ (e.g., equivalent to pyranometer measurements). The thick dash-dotted blue line represents the actual pyranometer measurements decomposed over wavelength as monochromatic radiation, based on spectrally averaged light attenuation coefficient (e.g., equivalent to k_{PAR}). Numbers on (b) indicate depth (0, 0.25, 0.5, 1, 2, and 3 m).

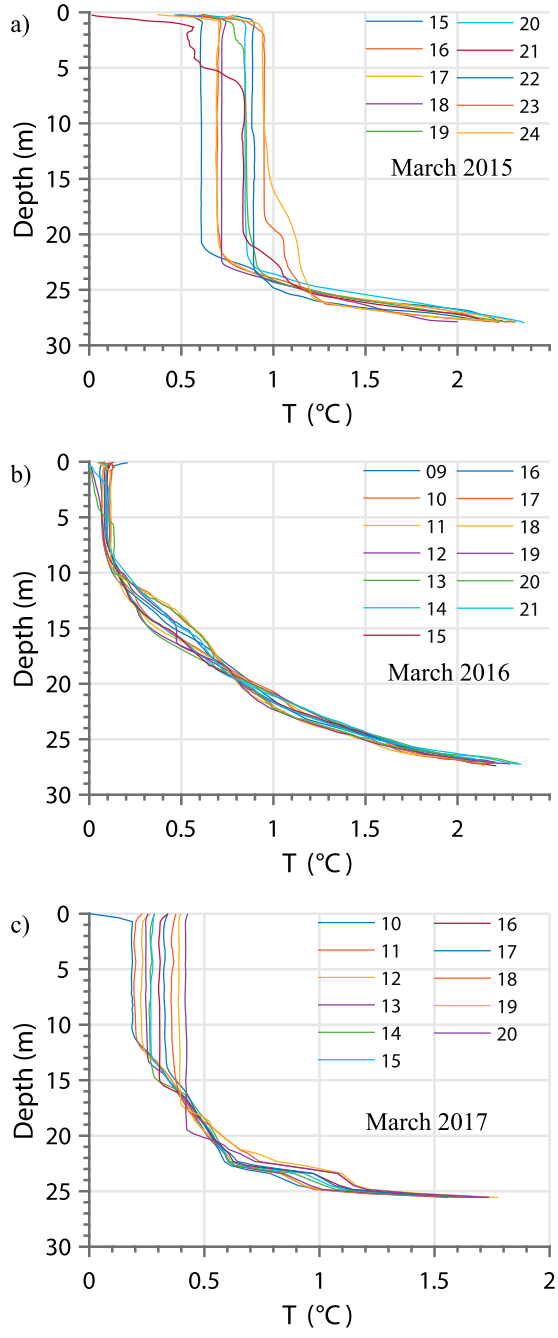

Figure 6. Examples of daytime vertical temperature profiles for 2015, 2016 and 2017. Each profile was taken at ~1600 h. Numbers in the legend represent successive days. The CML is significantly warming over time in March 2015 and 2017.

explained as a balance between vertical diffusion and the buoyancy flux (Kirillin and Terzhevik 2011).

Below the UIDL, the CML extended down to 10 m in 2016 as well as 20 m in 2015 and 2017 (Fig. 6). This layer was nearly constant in 2016 because of the weak radiative forcing and associated convection. In 2015, this layer was already ~20 m at the beginning of the measuring period, and the changes in the meteorological forcing affected the CML thickness (Fig. 6). The cause of this change was not investigated further in this study and is thereby briefly described here. From 20 to 25 March 2015, a storm affected the lake with strong wind from the northwest (Appendix B), which may have induced a pressure gradient that possibly led to horizontal transport and barotropic and/or baroclinic seiches within Petrozavodsk Bay. In March 2017, we observed a clear widening of h_{CML} from 12.2 to 20.5 m, equivalent to an average increase of 1.0 m d^{-1}. Not only h_{CML} varied, but also the temperature in the CML. For March 2015, T_{CML} started at 0.61 °C on 15 March and reached 0.95 °C on 24 March, with a mean

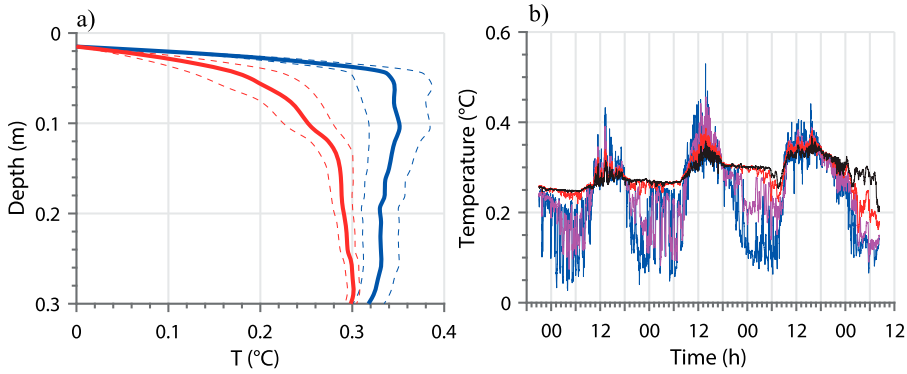

Figure 7. (a) Mean (bold line) and standard deviation (dashed lines) of temperature profiles in the UIDL during day (blue) and night (red) for 13 March 2017. (b) Three-day (13–15 March 2017) record of temperature in the UIDL at 3 cm (blue), 7.5 cm (pink), 16.5 cm (red), and 30 cm (black) depth. Note (1) day–night fluctuations, (2) high-frequency fluctuations, and (3) daytime unstable profiles.

daily increase of 0.04 °C d^{-1} (Fig. 6a, 8a). The temperature increase as well as the absolute temperature were smaller for March 2016, with an initial $T_{CML} = 0.07$ °C on 11 March, reaching $T_{CML} = 0.12$ °C on 23 March, and a mean daily increase of 0.0045 °C d^{-1} (Fig. 6b, 8b). For March 2017, T_{CML} started at 0.23 °C on 12 March and reached 0.42 °C on 20 March, with a mean daily increase of 0.024 °C d^{-1} (Fig. 6c, 8c).

Finally, we observed a stratified layer below the CML. The water column stability in the stratified layer below the CML was $N^2 = 8.5 \times 10^{-5}$ s^{-2} in 2015, 4.3×10^{-5} s^{-2} in 2016, and 1.2×10^{-5} s^{-2} in 2017.

Temporal change of the mixed layer thickness

Data collected in 2017 allowed investigating the temporal change of h_{CML} as a function of B_*. Equation 1 applied to the March 2017 data agreed well with the observed h_{CML} (Fig. 8c; root mean square error [RMSE] = 1.1 m, R^2 = 0.65). Yet, the model could not reproduce the oscillations in h_{CML} identified during the second part of the measuring period resulting from other processes such as deep large-scale motions not investigated here. Other studies have shown that river intrusions (Cortés et al. 2017) or differential horizontal heating (Kirillin et al. 2015) can cause spatio-temporal variability in the locally measured temperature. Equation 1 allows examining whether radiatively driven convective turbulence is the main process, and significant deviations from equation 1 suggest that additional physical mechanisms might be relevant for the CML evolution. The most relevant parameters, incoming light, optical properties, and CML characteristics, were summarized for the 3 measuring periods (Table 1).

Convective velocity

In 2016, the downward-looking 600 kHz ADCP showed a diurnal pattern with alternating downward and upward velocities ranging up to ±2.5 mm s^{-1} during daytime (Fig. 9a). The distribution of the plumes was asymmetrical with mostly downward thermal plumes recorded on 16 March and mostly upward thermal plumes recorded on the 22 March. Plume median duration was: τ_c ~17 (SD 9) min.

The situation was much clearer in 2017, where all ADCPs showed alternating downward and upward plumes during daytime reaching up to ±7.5 mm s^{-1} (Fig. 9b–c). The distribution was asymmetrical, with larger velocities recorded for downward plumes than for upward plumes (Fig. 9d). When compared to $\overline{w_*}$, we obtained $\overline{w_*} = \beta w^+ = -\gamma w^-$, with $\beta = 1.25$ and $\gamma = 0.75$. Indices "+" and "–" are for upward and downward velocities. From the continuity equation balance, we obtain: $\frac{\tau_c^-}{\tau_c^+} = \frac{\gamma}{\beta} \sim 0.6$, with τ_c^+ (respectively τ_c^-) the duration of upward (respectively downward) convective plumes. The skewness in the distribution indicates that the CML is slightly dominated (by ~60%) by slowly rising upward flow. Our observations agree with previous large eddy simulation of near-surface cooling-induced convection (Sander et al. 2000).

From the vertical velocity observations, the onset and breakdown of the radiatively driven convection can be estimated. The median time lag between sunrise and onset of convection was 90 (SD 40) min. A threshold approach on the slowly decaying convective turbulence is arbitrary, yet the same approach applied to sunset (10 W m^{-2}, ~1830 h, local time) gives a time lag of 225 (SD 65) min.

Discussion

Convective velocity

The convective velocity was estimated for 3 late winter periods based on equations 2 and 3. This parameterization was compared to the direct measurements of the vertical velocity in March 2017, using equation 4 (Fig. 10a).

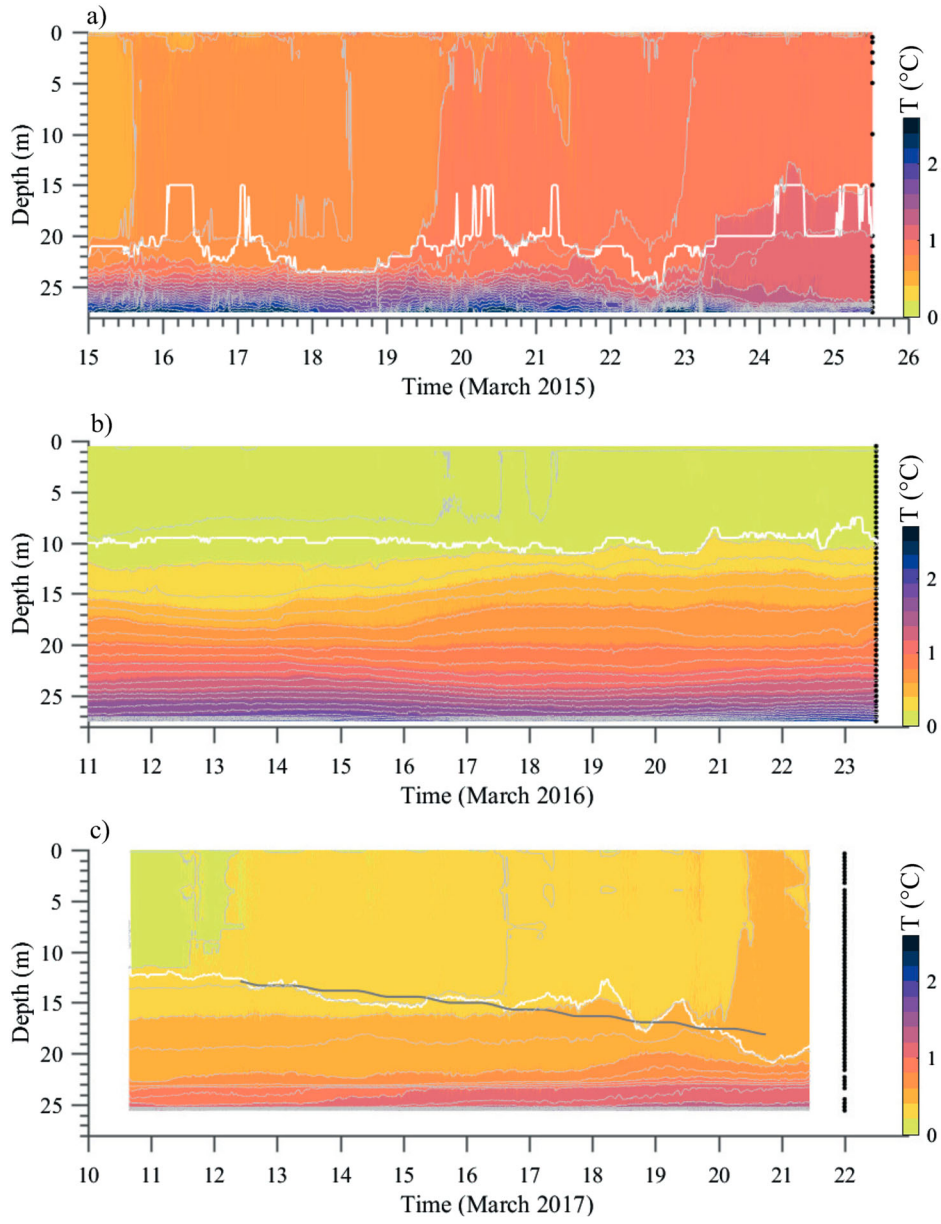

Figure 8 . Temporal evolution of the temperature (°C) over the water column for (a) 2015, (b) 2016, and (c) 2017. The black dots on the right indicate the location of the sensors. The grey lines represent isotherms (ΔT = 0.1 °C). White lines represent the lower end of h_{CML}. The black line on panel (c) represents the modelled temporal change of the CML.

Excellent agreement (Fig. 10b, RMSE = 0.67 mm s^{-1}, R^2 = 0.51) occurred at midday between the direct and the buoyancy flux method, the envelope of the direct measurements (Fig. 10a). The same method was applied for March 2016 under weaker convection and provided a way to compare the observed convective velocity from ADCP measurements with the scaling using the monochromatic radiation assumption (e.g., PAR sensor, blue dots and line in Fig. 10b) and the spectrally resolved radiation method (e.g., hyperspectral measurements). Our results suggest

Table 1. Mean and standard deviation (SD) of measured parameters (light, optical characteristics, and CML properties) during the 3 late winter periods in 2015, 2016, and 2017.

	$E_d(0^+)$ (W m^{-2})	$E_d(0^-)$ (W m^{-2})	A (–)	T_r (–)	k_{PAR} (m^{-1})	k_λ (m^{-1})	h_{CML} (m)	dh_{CML}/dt (m s^{-1})	dT_{CML}/dt (°C s^{-1})
2015	345 (132)	108 (50)	0.23 (0.18)	0.42 (0.14)	1.2	—	20	—	0.04
2016	351 (143)	6 (3)	0.71 (0.05)	0.07 (0.03)	3.2	2.6	9	—	0.0045
2017	262 (113)	79 (25)	0.21 (0.1)	0.40 (0.05)	2.6	—	12–20	1.0	0.024

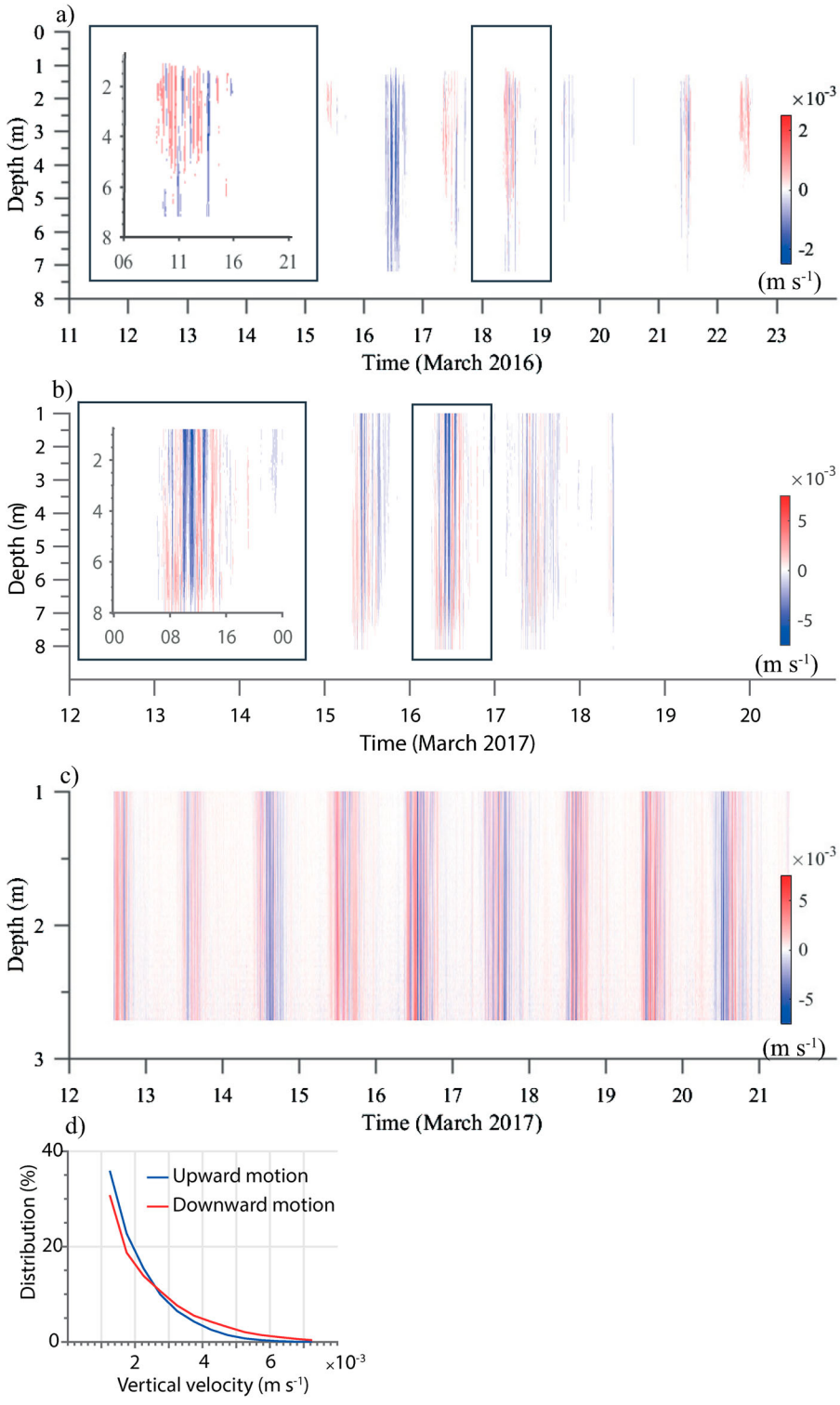

Figure 9. Vertical velocity for (a) 2016 and (b, c) 2017. (a, b) Data from a 600 kHz Mode 11 RDI ADCP. (c) Data from a 2000 kHz Pulse-coherent Nortek Aquadopp ADCP. In 2017, the RDI (b) only worked for 3 days. Left insets in panels (a) and (b) are zooms for 18 March 2016 and 17 March 2017 (x-axis in hours on the inset) showing alternating upward and downward thermal plumes. (d) Distributions of upward and downward velocities of convective plumes.

an improvement in the estimation of the convective velocity scale by using the spectrally resolved radiation method (RMSE = 0.32 mm s^{-1}, $R^2 = 0.65$ vs. RMSE = 0.35 mm s^{-1}, $R^2 = 0.25$). We showed that the directly measured convective velocity had a slower decay rate than the velocity estimate based on the buoyancy flux method, in which low convective velocities were recorded during the evening and early night (no light). From a sunset occurring at 0630 h

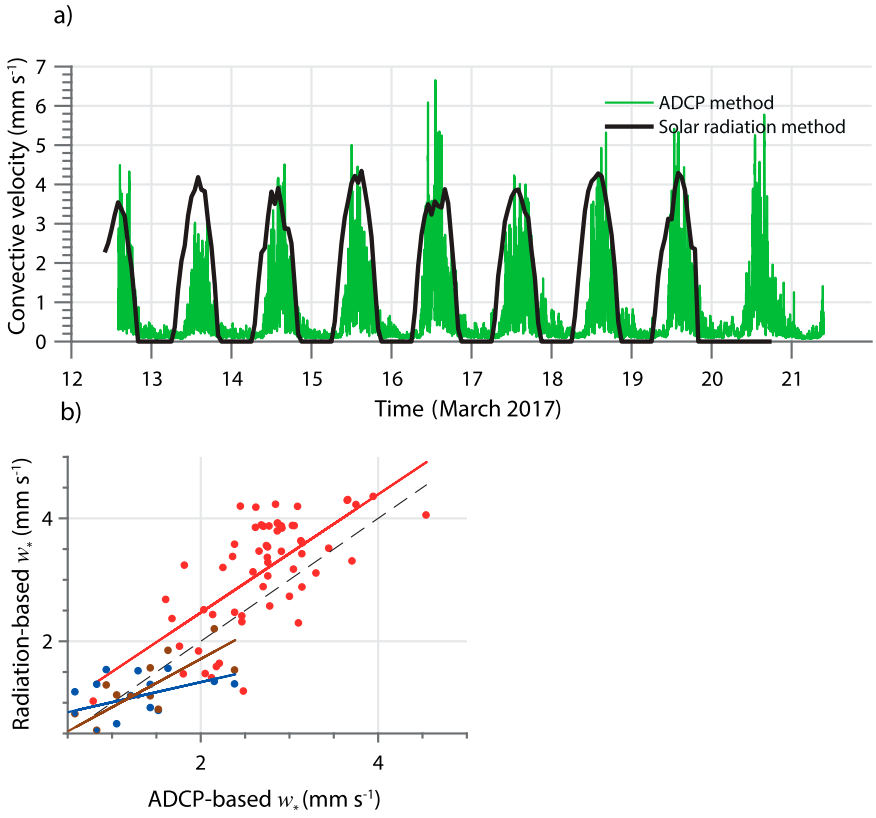

Figure 10. (a) Temporal evolution of the ADCP-based (green, equation 4) and radiation-based estimates (black line, equation 3) of the convective velocity scale for March 2017. (b) Comparison of the 2 methods at midday (1100 to 1400 h) for March 2017 (red dots and line), March 2016 using PAR and pyranometer sensors (blue dots and line), and March 2016 using hyperspectral radiometer (brown dots and line). The dashed-line indicates the 1:1 relation.

during the March 2017 measurements, the median breakdown time for the convective turbulence was at 1015 h (i.e., 225 [SD 65] min after sunset). The onset of the morning convection was also shifted. The buoyancy flux method responded immediately to the onset of solar radiation after sunrise while the measured velocities exceeded the threshold by 90 (SD 17) min later. Although the decaying convective turbulence has been previously investigated (Nieuwstadt and Brost 1986, Bouffard et al. 2016), our observations confirm the systematic delay in the onset of convection, and we conclude that estimates of the daytime duration using solar radiation largely underestimate the duration of the convection.

Relevance of spectral light extinction estimates

Under-ice stratification in freshwaters (low salinity) is governed by the density increase with temperature until the temperature of maximum density is reached. For $T < T_{MD}$, solar radiation increases the near-surface water density and leads to gravitational instabilities and convection. There is a misleading symmetry with the case $T > T_{MD}$, in which surface cooling drives gravitational instabilities. The heat leaving the lake during the cooling phase is strictly located in the top millimetre of the air–water interface while the shortwave solar radiation responsible for the warming is deposited in the interior of the water column. In clear freshwaters, short wavelengths penetrate deeper than long wavelengths, and convective mixing resulting from near-surface heating requires an accurate description of the incoming solar radiation (Kirillin et al. 2012).

The 3 late winter observations present different patterns for the convective velocity. The parameterized velocity was strong in 2015 and 2017 and weak in 2016, yet the strength of the convective turbulence was not correlated to the incoming solar radiation, which was higher in 2016 (Fig. 2). Albedo and transmittance in the few centimetres of thick snow and white ice cover drastically damped the energy input in 2016 compared to 2015 and 2017 (Fig. 3, 4). This example demonstrates the inability of estimating the buoyancy flux based on above-ice solar radiation measurements only.

The volumetric forcing of solar radiation in the photic zone requires accurate description of the light absorption across the upper water column. We compared the buoyancy flux estimates from light extinction coefficients based on a k_{PAR} and a second estimate based on a full

wavelength decomposition of k_λ from underwater hyperspectral measurements. The second approach led to $\overline{k_\lambda}$ = 2.6 m^{-1} for March 2016, representing the average over $400 < \lambda < 700$ nm (Fig. 5), which differs from $k_{PAR} = 3.2$ m^{-1} estimated with PAR sensors at the same time (16 March 2400 h; 2016). We removed potential sensors bias by setting $k_{PAR} = \overline{k_\lambda}$. For this period, we obtained B_{*PAR} = 2.1 × 10^{-9} W kg^{-1} (monochromatic radiative transfer assumption) and $\widetilde{B}$ = 6.4 × 10^{-9} W kg^{-1} (wavelength dependent radiative transfer) with an error of 67% from the corrected PAR estimate. The difference reached 80% for the uncorrected (e.g., $k_{PAR} = 3.2$ m^{-1}) PAR estimate. The error reached 31% for the convective velocity using the corrected PAR and 40% using the uncorrected PAR. CDOM modifies the spectral distribution (Röttgers and Doerffer 2007) of the light absorption compared to PAR-based light absorption. Many high latitude ice-covered lakes are CDOM-dominated, and spectral correction may be required to accurately quantify radiatively driven under-ice convection. In addition to the varying light absorption by the particles, the ice itself modifies the heat input into the water below (Jakkila et al. 2009, Zdorovennova et al. 2013b). We conclude that not only under-ice downwelling irradiance is required but also information regarding the spectrally resolved absorption.

Given the high absorption and the large thickness of CML, B_* and w_*were not sensitive to the lower boundary of CML as would be the case in the early stage of convection or in clear lakes where the light penetration may scale with the CML. Yet B_* and w_*depend on the thickness of UIDL. Over daytime for 16 March 2016 we observed a 10 cm variability in δ (e.g., 66% change) leading to a change in B_* and w_* of 24% and 7%, respectively (for the case described in Fig. 5). The difference reached 36% and 12%, respectively, when B_* and w_* were calculated with h_{CML} starting at $z = 0$ (UIDL neglected).

Minimum setup for in situ analysis of radiatively driven convection

From this study, we inferred a minimum setup required to quantify under-ice convection. The 2 main parameters were h_{CML} and B_*. We developed indications of the errors from inaccuracy in (1) radiation and absorption in the water column, (2) estimates of the upper boundary of the CML, and (3) use of the radiatively driven buoyancy flux parameterization (equation 3). While repeated CTD profiles provide sufficient information to quantify the extent of the CML, the upper boundary of the convective layer (where a large part of the heat is deposited) must be precisely determined. Above the CML, the absorbed heat stabilizes the UIDL, whereas in the CML the solar radiation drives the convective turbulence. While the long-term goal is to infer the convection from the incoming solar radiation, the high variability of the ice properties hinders any attempt to link atmospheric forcing directly to under-ice convection. A radiometer for downwelling irradiance just under the ice is thereby required. Depending on the temporal variability, the light extinction in the water column can be estimated from single radiometer profiles (PAR or hyperspectral sensors). In CDOM-dominated lakes, the estimated error in using a PAR sensor instead of a spectrally resolving sensor can reach ~40% for w_*.

Implications for "life under the ice"

To show the significance of adequate quantification of the radiative convection within the CML, we exemplified the implications for phytoplankton growth. We assumed that under-ice phytoplankton growth was light-limited (Hampton et al. 2017) and that the increase of solar radiation in late winter, responsible for radiatively driven convection, thereby also promotes phytoplankton growth. Salmi et al. (2014) observed a slight increase of the biomass of picophytoplankton (<2 μm) under convective conditions during late-winter ice-covered conditions in Lake Vesijärvi. Twiss et al. (2014) measured a rate of growth equivalent to the rate of loss of phytoplankton under ice in Lake Erie. Kelley (1997) suggested that convective turbulence could reduce sedimentation of nonmotile phytoplankton such as diatoms, which are often dominant species in early spring. The potential of convective turbulence to reduce sedimentation was parameterized as a function of w_*, the phytoplankton settling velocity w_s, and a suspension efficiency. This simple model could justify the phytoplankton growth observed under the ice in Lake Baikal (Kelley 1997). Yet, the model developed by Kelley (1997) is not easy to use, and some physical assumptions were also questioned by Mironov et al. (2002).

Here, we present a simple heuristic model to evaluate how radiatively driven under-ice convection can favour the growth of nonmotile phytoplankton. We defined a net daily rate of change of phytoplankton as $\frac{C^{n+1} - C^n}{C^n}$, where C is the concentration of phytoplankton in the CML and n-index denotes the day number n. The sedimentation velocity of nonmotile phytoplankton is given by w_s. We further assumed a light-limited growth rate of phytoplankton with $P_G^{max} = f(E_d)$, the maximum growth rate in the upper part of the CML, where E_d is maximal. Given the mixing properties of the radiatively driven convective turbulence, we assumed that the phytoplankton population will be advected into the upper part of the CML for a time long enough to insure sufficient exposure time for phytoplankton in the photic zone, thereby ensuring P_G^{max} to the whole

phytoplankton community within the CML. The daily evolution of C^n was divided into 2 phases: a phase with active convection, τ_c^n (mostly during daytime) and a phase with no convection, τ_{nc}^n, with $\tau_c^n + \tau_{nc}^n = 1$ d. We derived the minimal values of physical properties (e.g., w_*, h_{CML} and τ_c^n) that would favour or hamper growth of nonmotile phytoplankton characterized by P_G^{max} and w_s. Note that the controlling physical parameters were all determined by the volumetric buoyancy flux working in the CML and can thereby be estimated as a function of solar radiation and light absorption (detailed calculation and assumptions in Appendix C). From this model, a (positive) daily growth rate, $\frac{C^{n+1} - C^n}{C^n} > 0$, leads to:

$$\left[P_G^{\max}(\bar{w}_* - w_s)\frac{1}{2}\tau_c - w_s\tau_{day}\right] > 0, \qquad (5)$$

with $\tau_{day} = 1$. Equation 5 does not take into account any biological processes and provides no representative value regarding the growth rate. Yet it expresses the conditions for which radiatively driven convection is not strong enough to sustain a positive growth rate of nonmotile phytoplankton.

When applied to conditions observed in 2017 (h_{CML} = 15 m, $\tau_c^n = 0.5$ d, $\bar{w}_* = 2.5$ mm s^{-1}), we estimated the minimal growth rate, P_G^{max}, needed for a given sinking speed, w_s (Fig. 11). The growth rate was consistent with observations from Lake Erie (Twiss et al. 2014), and w_s was within the range of diatom sinking speed, 0.2 to 20 m d^{-1} (Miklasz and Denny 2010). The influence of w_*on the development of nonmotile phytoplankton, defined by 2 parameters (P_G^{max} and w_s), was determined (Fig. 11b). This heuristic model offers a simple methodology to evaluate the role of convective processes on nonmotile phytoplankton growth.

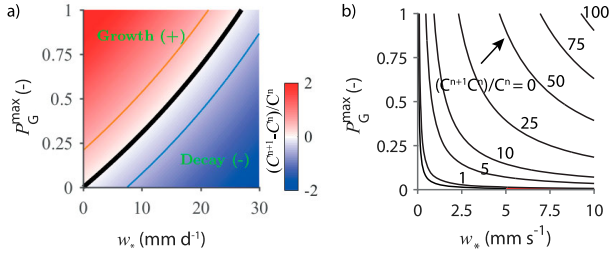

Figure 11. (a) Estimated daily phytoplankton growth based on equation 5 as a function of the nonmotile phytoplankton sinking speed w_s and maximum growth rate P_G^{max}. The area above the white curve indicates condition favourable for phytoplankton growth. The physical values correspond to the in situ conditions in 2017 with h_{CML} = 15 m, w_* = 2.5 mm s^{-1} and τ_c^n = 0.5 d. (b) Estimated daily phytoplankton growth as a function of the convective velocity w_* and maximum growth rate P_G^{max} for different sinking velocities (1–100 m d^{-1}). As an illustration, large particles with high sinking speed (w_s > 25 m d^{-1}) will not be maintained in the CML for w_* = 2.5 mm s^{-1} but will likely be in a more favourable environment for w_* > 5 mm s^{-1}.

Conclusion

We analysed the in situ data from 3 consecutive late winter (Mar) under-ice conditions in Lake Onego. The 3 measurement periods significantly differed from each other in terms of atmospheric and ice/snow conditions directly affecting the under-ice convection. We first showed that, despite the weak velocities of the radiatively driven convective turbulence, the large-scale thermal plumes can be directly measured with pulse-coherent ADCPs. The direct measurements were in good agreement with the classical buoyancy flux parameterization of the convective scale; however, the classical parameterization could not reproduce the duration of the daily convection, τ_c. Indeed, we noticed a ~1.5 h delay between sunrise and onset of convection, and a ~3.5 h delay between sunset and decay of convection. We showed that all relevant parameters (h_{CML}, B_*, $\partial T_{CML}/\partial t$, τ_c, and w_*) could be directly accessed from temperature and radiometer sensors and provided a minimum in situ setup to access these parameters together with errors estimates. Interestingly, these parameters all depend on solar radiation and optical properties of snow, ice, and the water column. Thereby, the vertical distribution of heat in the water column is the cornerstone for quantifying radiatively driven convection. Further investigations of spectrally resolved light absorption and UIDL dynamics will help to better constrain the analysis of radiatively driven under-ice convection. In this study, we showed that the physical boundary conditions for biological models can be accurately measured. Finally, we provided a simple heuristic model to evaluate the role of under-ice convection for nonmotile phytoplankton growth.

Acknowledgements

This study was supported by the FEEL Foundation, "Fondation pour l'Etude des Eaux du Léman." The authors thank Andrey Mitrokhov, Andrey Georgiev, Alexey Tolstikov, and Andrey Balagansky (Northern Water Problems Institute, Karelian Research Centre, Russian Academy of Science) and Michael Plüss (Eawag) for their efforts in collecting observational data. We also thank Vasili Kovalenko, the head of the Russian expedition, and Natacha Pasche from the Limnology Center (EPFL) for the logistic and financial support.

ORCID

Damien Bouffard http://orcid.org/0000-0002-2005-9718
Galina Zdorovennova http://orcid.org/0000-0003-2726-0104
Sergey Bogdanov http://orcid.org/0000-0003-4150-2712
Tatyana Efremova http://orcid.org/0000-0003-0313-6731
Nikolay Palshin http://orcid.org/0000-0003-1540-3788
Arkady Terzhevik http://orcid.org/0000-0002-0837-9065

Sergey Volkov http://orcid.org/0000-0002-5385-1541
Alfred Wüest http://orcid.org/0000-0001-7984-0368
Roman Zdorovennov http://orcid.org/0000-0003-1695-4872
Hugo N. Ulloa http://orcid.org/0000-0002-1995-6630

References

Bengtsson L. 1996. Mixing in ice-covered lakes. Hydrobiologia. 322:91–97.

Bluteau CE, Pieters R, Lawrence GA. 2017. The effects of salt exclusion during ice formation on circulation in lakes. Environ Fluid Mech. 17:579–590.

Bouffard D, Wüest A. 2019. Convection in lakes. Annu Rev Fluid Mech. 51:189–215.

Bouffard D, Zdorovennov RE, Zdorovennova GE, Pasche N, Wüest A, Terzhevik AY. 2016. Ice-covered Lake Onega: effects of radiation on convection and internal waves. Hydrobiologia. 780:21–36.

Cortés A, MacIntyre S, Sadro S. 2017. Flowpath and retention of snowmelt in an ice-covered arctic lake. Limnol Oceanogr. 62:2023–2044.

Deardorff JW. 1970. Convective velocity and temperature scales for the unstable planetary boundary layer and for Rayleigh convection. J Atmos Sci. 27:1211–1213.

Ducharme-Riel V, Vachon D, Del Giorgio PA, Prairie YT. 2015. The relative contribution of winter under-ice and summer hypolimnetic CO_2 accumulation to the annual CO_2 emissions from northern lakes. Ecosystems. 18:547–559.

Farmer DM. 1975. Penetrative convection in the absence of mean shear. QJR Meteorol Soc. 101:869–891.

Forrest AL, Laval BE, Pieters R, Lim DS. 2008. Convectively driven transport in temperate lakes. Limnol Oceanogr. 53:2321–2332.

Forrest AL, Laval BE, Pieters R, Lim DSS. 2013. A cyclonic gyre in an ice-covered lake. Limnol Oceanogr. 58:363–375.

Golosov S, Maher OA, Schipunova E, Terzhevik A, Zdorovennova G, Kirillin G. 2007. Physical background of the development of oxygen depletion in ice-covered lakes. Oecologia. 151:331–340.

Hampton SE, Galloway AWE, Powers SM, Ozersky T, Woo KH, Batt RD, Labou SG, O'Reilly CM, Sharma S, Lottig NR, et al. 2017. Ecology under lake ice. Ecol Lett. 20:98–111.

Jakkila J, Leppäranta M, Kawamura T, Shirasawa K, Salonen K. 2009. Radiation transfer and heat budget during the ice season in Lake Pääjärvi, Finland. Aquat Ecol. 43:681–692.

Jonas T, Terzhevik AY, Mironov DV, Wüest A. 2003. Radiatively driven convection in an ice-covered lake investigated by using temperature microstructure technique. J Geophys Res. 108:3183.

Katz SL, Izmest'eva LR, Hampton SE, Ozersky T, Shchapov K, Moore MV, Shimaraeva SV, Silow EA. 2015. The "Melosira years" of Lake Baikal: winter environmental conditions at ice onset predict under-ice algal blooms in spring. Limnol Oceanogr. 60:1950–1964.

Kelley DE. 1997. Convection in ice-covered lakes: effects on algal suspension. J Plankton Res. 19:1859–1880.

Kirillin G, Leppäranta M, Terzhevik A, Granin N, Bernhardt J, Engelhardt C, Efremova T, Golosov S, Palshin N, Sherstyankin P, et al. 2012. Physics of seasonally ice-covered lakes: a review. Aquat Sci. 74:659–682.

Kirillin G, Terzhevik A. 2011. Thermal instability in freshwater lakes under ice: effect of salt gradients or solar radiation? Cold Reg Sci Technol. 65:184–190.

Kirillin GB, Forrest AL, Graves KE, Fischer A, Engelhardt C, Laval BE. 2015. Axisymmetric circulation driven by marginal heating in ice-covered lakes. Geophys Res Lett. 42:2893–2900.

Lei R, Leppäranta M, Erm A, Jaatinen E, Pärn O. 2011. Field investigations of apparent optical properties of ice cover in Finnish and Estonian lakes in winter 2009. Est J Earth Sci. 60:50–64.

Leppäranta M, Reinart A, Erm A, Arst H, Hussainov M, Sipelgas L. 2003. Investigation of ice and water properties and under-ice light fields in fresh and brackish water bodies. Hydrol Res. 34:245–266.

Leppäranta M, Terzhevik A, Shirasawa K. 2010. Solar radiation and ice melting in Lake Vendyurskoe, Russian Karelia. Hydrol Res. 41:50–62.

Malm J, Bengtsson L, Terzhevik A, Boyarinov P, Glinsky A, Palshin N, Petrov M. 1998. Field study on currents in a shallow, ice-covered lake. Limnol Oceanogr. 43:1669–1679.

Miklasz KA, Denny MW. 2010. Diatom sinking speeds: improved predictions and insight from a modified Stokes' law. Limnol Oceanogr. 55:2513–2525.

Mironov D, Terzhevik A, Kirillin G, Jonas T, Malm J, Farmer D. 2002. Radiatively driven convection in ice-covered lakes: observations, scaling, and a mixed layer model. J Geophys Res. 107:7–16.

Nieuwstadt FTM, Brost RA. 1986. The decay of convective turbulence. J Atmos Sci. 43:532–546.

Pernica P, North RL, Baulch HM. 2017. In the cold light of day: the potential importance of under-ice convective mixed layers to primary producers. Inland Waters. 7:138–150.

Petrov MP, Terzhevik AY, Palshin NI, Zdorovennov RE, Zdorovennova GE. 2005. Absorption of solar radiation by snow-and-ice cover of lakes. Water Resour. 32:496–504.

Powers SM, Hampton SE. 2016. Winter Limnology as a new frontier. Limnol Oceanogr Bull. 25:103–108.

Röttgers R, Doerffer R. 2007. Measurements of optical absorption by chromophoric dissolved organic matter using a point-source integrating-cavity absorption meter. Limnol Oceanogr-Meth. 5:126–135.

Sabylina AV, Ryzhakov AV. 2018. Hydrochemical characteristic of the littoral zone of Lake Onega. Water Resour. 45:213–221.

Salmi P, Lehmijoki A, Salonen K. 2014. Development of picoplankton during natural and enhanced mixing under late-winter ice. J Plankton Res. 36:1501–1511.

Sander J, Simon A, Jonas T, Wüest A. 2000. Surface turbulence in natural waters: a comparison of large eddy simulations with microstructure observations. J Geophys Res Oceans. 105:1195–1207.

Twiss MR, Smith DE, Cafferty EM, Carrick HJ. 2014. Phytoplankton growth dynamics in offshore Lake Erie during mid-winter. J Great Lakes Res. 40:449–454.

Ulloa HN, Wüest A, Bouffard D. 2018. Mechanical energy budget and mixing efficiency for a radiatively heated ice-covered waterbody. J Fluid Mech. 852:R1.

Zdorovennova G, Zdorovennov R, Palshin N, Terzhevik A. 2013a. Optical properties of the ice cover on

Vendyurskoe Lake, Russian Karelia (1995–2012). Ann Glaciol. 4:121–124.
Zdorovennov R, Palshin N, Zdorovennova G, Efremova T, Terzhevik A. 2013b. Interannual variability of ice and snow cover of a small shallow lake. Est J Earth Sci. 61:26–32.
Zilitinkevĭc SS. 1991. Turbulent penetrative convection. Aldershot (UK): Avebury Technical.

Appendix A

Sensors

Temperature (°C)

CTD-90 Sea&Sun Technology

Accuracy: ±0.005 °C; *resolution*: ±0.001 °C

Setup: 1 profile per hour; each year

TR-1060 RBR

Accuracy: ±0.002 °C; *resolution*: ±0.00005 °C

Setup: 10 s sampling frequency

2015: depth (m) = [0, 0.5, 1, 2, 3, 5 10, 15, 20, 21, 22, 22.5, 23, 23.5, 24, 24.5, 25, 25.5, 26, 26.5, 27, 27.5]

2016: depth (m) = [0: 0.025: 0.25]

depth (m) = [0, 0.5, 1, 2, 3, 5 10, 15, 20, 21, 22, 22.5, 23, 23.5, 24, 24.5, 25, 25.5, 26, 26.5, 27, 27.5]

2017: depth (m) = [0: 0.025: 0.25]

depth (m) = [0: 0.36: 25.6]

Solar radiation (W m^{-2})

Pyranometer M80

Accuracy: ±10%; *resolution*: 0.2 W m^{-2}

Setup: 3 pyranometers. 2 pyranometers above the ice for downwelling $E_d(0^+)$ and upwelling $E_u(0^+)$ irradiance (star-shaped pyranometers) and 1 pyranometer (M80) under the ice for downwelling irradiance $E_d(0^-)$; 1 min sampling; each year.

Light intensity PAR sensors (µm m^{-2} s^{-1})

Light intensity recorder MDS-MkV/L, Alec Electronics

Accuracy: ±4% FS; *resolution*: 1 µm m^{-2} s^{-1}

Setup: 9 sensors; 1 min sampling

2015: 1 m spacing between 0–8 m

2016: 1 m spacing between 0–8 m

2017: depth (m) = [0, 0.35, 0.6, 0.85, 1.1, 1.6, 2.1, 2.6]

Irradiance (µW m^{-2} mm^{-1})

Hyperspectral radiometer (Ramses Trios)

Wavelength range [lower wavelength : resolution : larger wavelength] [320 nm : 3 nm : 950 nm]; *wavelength accuracy*: 0–3 nm; *number of channels*: 190

Setup: 1 profile per hour between 1100 and 1500 h. A profile is made up of 3 min measurements at depth 0, 0.5, 1, 1.5 m

Acoustic Doppler Current Profiler; Velocity (m s^{-1})

Aquadopp, Nortek

Setup: facing downward, frozen into the ice with head immediately underneath the ice

Year 2016: *Ping number:* 512 or 2048; *Ensemble interval*: 600 s; *Blanking distance*: 0.1 m; *Number of bins*: 38; *Bin size*: 0.05 m

Year 2017: *Ping number*: 30; *Ensemble interval*: 60 s; *Blanking distance*: 0.1 m; *Number of bins*: 126; *Bin size*: 0.02 m

RDI, Teledyne 600 kHz Mode 11

Setup: facing downward, frozen into the ice with head immediately underneath the ice

Ping number: 596; *Ensemble interval*: 300 s; *Blanking distance*: 0.29 m; *Number of bins*: 78; *Bin size*: 0.10 m

Appendix B

Meteorological forcing

During the observation period in 2015, the meteorological conditions were divided into 2 periods. From 14 to 19 March, air temperature, T_a, oscillated between −5 and 8 °C (mean T_a = 1.1 °C) with weak wind condition (<4 m s^{-1}, mean 1.4 m s^{-1}; Fig. B1). The situation changed on 19 March with a strong decrease in air temperature to −10 °C (mean T_a = −3.5 °C) and a strong wind reaching 10 m s^{-1} (mean 5.3 m s^{-1}). The meteorological forcing from the observation period in 2016 can also be divided into 2 periods (Fig. B2). From 10 to 17 March, T_a oscillated between −4 and 4 °C (mean T_a = −0.1 °C) and then

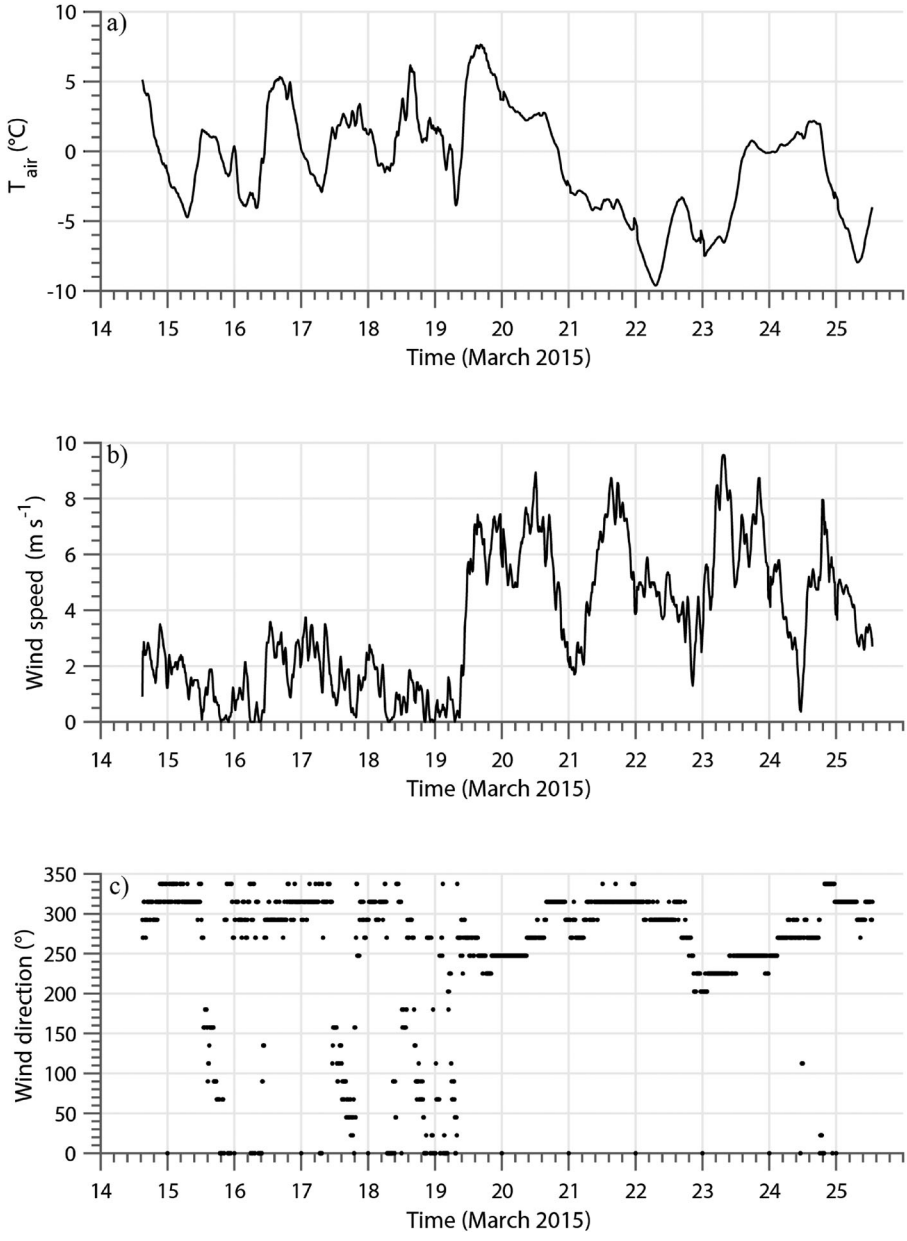

Figure B1. Meteorological conditions for the measuring period in March 2015 with (a) air temperature, (b) wind speed, and (c) wind direction. All measurements were taken on a meteorological mast mounted on the ice a few meters from the moorings.

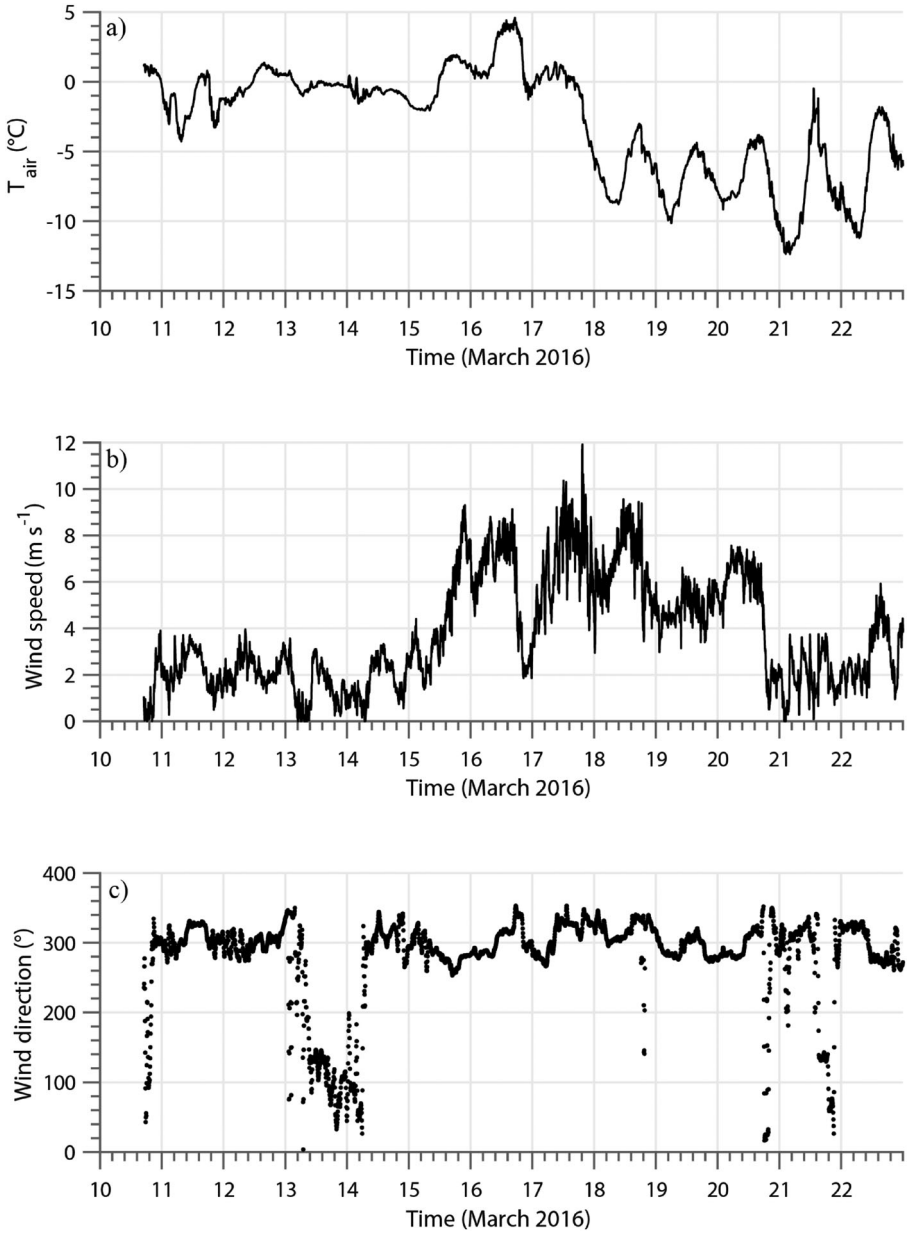

Figure B2. Meteorological conditions for the measuring period in March 2016 with (a) air temperature, (b) wind speed, and (c) wind direction. All measurements were taken on a meteorological mast mounted on the ice a few meters from the moorings.

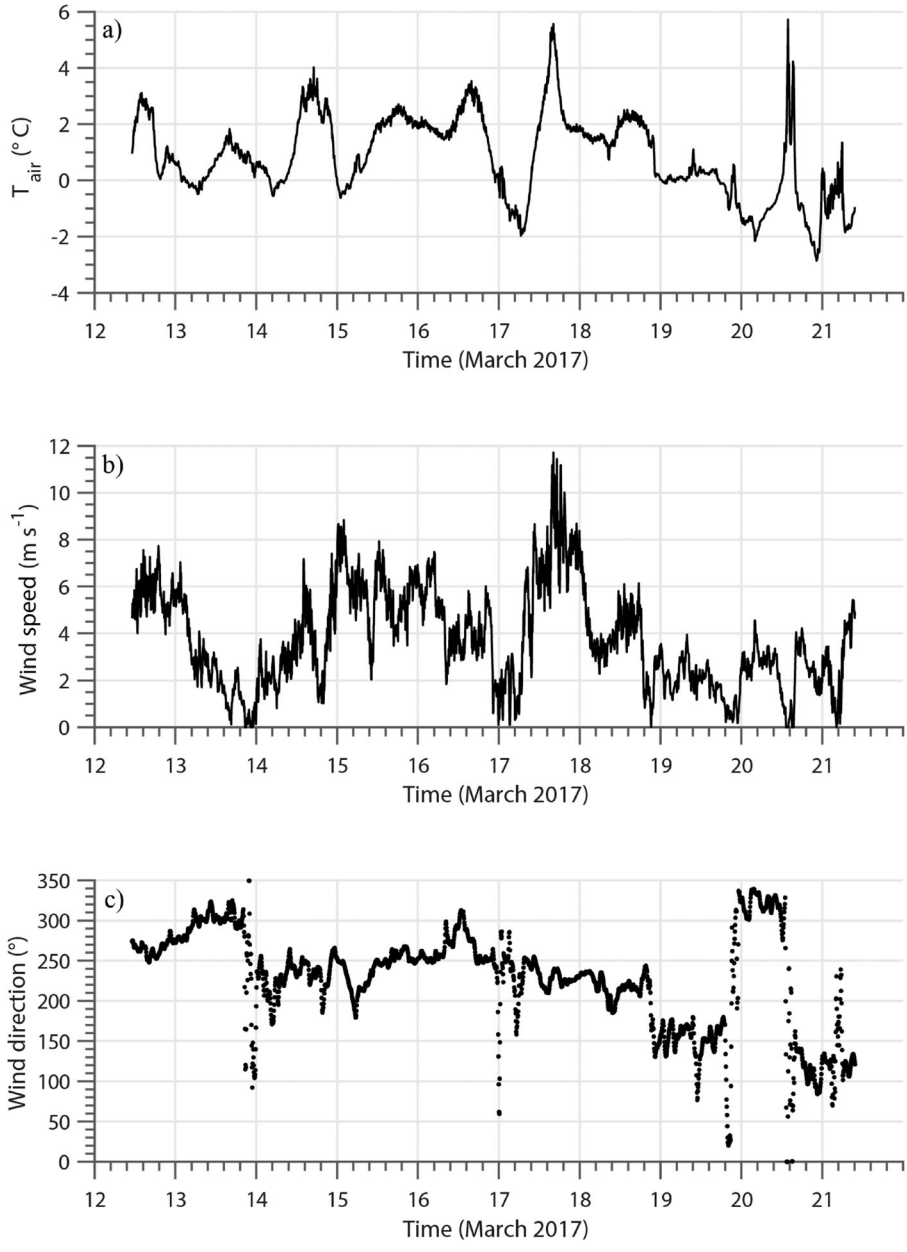

Figure B3. Meteorological conditions for the measuring period in March 2017 with (a) air temperature, (b) wind speed, and (c) wind direction. All measurements were taken on a meteorological mast mounted on the ice a few meters from the moorings.

between −13 and −1 °C (mean $T_a = -5.9$ °C) for the 5 following days. The wind remained weak during 10–15 March (mean 2.0 m s^{-1}) and then increased to a mean intensity of 6.1 m s^{-1} during 15–20 March. Finally, the meteorological conditions for the observation period in 2017 remained comparatively constant, with T_a oscillating between –3 and 6 °C (mean $T_a = 0.9$ ° C) with a relatively strong wind event on 17 March (~10 m s^{-1}; Fig. B3).

Appendix C

The algal-growth model introduced in "Implications for life under the ice" is based on the following assumptions:

1. A net daily rate of change of phytoplankton $\frac{C^{n+1}}{C^n} > 1$ or $\frac{C_n^{n+1} - C_n^n}{C^n} > 0$, where n-index denotes the day n, represents phytoplankton "growth."
2. A constant sedimentation velocity for nonmotile phytoplankton, w_s.
3. A light-limited growth rate of phytoplankton with P_G^{max}, the maximum growth rate in the upper region of CML where E_d under the ice is maximal. Yet, given the mixing properties of the radiatively driven convective turbulence, we assumed that the entire

population of phytoplankton was advected for a time long enough into the upper region of the CML to ensure that all phytoplankton in the CML are controlled by a P_G^{max}.

4. A uniform vertical distribution of nonmotile phytoplankton, C^n, in the CML. This assumption provided a conservative estimate of the net growth rate as, despite the convective turbulence, we expected more phytoplankton in the growing zone (e.g., upper CML) and less in the sinking zone (e.g., lower CML).
5. A daily evolution of C^n divided into 2 periods, a period with active convection, τ_c^n (mostly during daytime) and a period with no convection, τ_{nc}^n, with $\tau_c^n + \tau_{nc}^n = 1$.
6. A diurnal-averaged convective velocity, $\bar{w}_*$, in the CML with an upward and downward phase satisfying the volume balance condition: $S\bar{w}^{n+}\tau_c^{n+} = S\bar{w}^{-}\tau_c^{n-}$, $\tau_c^+ + \tau_c^- = \tau_c$, over an area S. Indices "+" and "–" are for upward and downward velocities, respectively. We assumed that only maximal rate of growth in the upward mass flux stays in the convective cell. If we consider that $\bar{w}_*^- = -\beta\bar{w}_*$ and $\bar{w}_*^+ = +\gamma\bar{w}_*$ then from the volume balance we obtained: $\tau_c^+ = \dfrac{\beta}{\beta+\gamma}\tau_c$, $\tau_c^- = \dfrac{\gamma}{\beta+\gamma}\tau_c$.
7. The change in C^n due to the deepening of the CML was negligible (decrease in C^n from the deepening together with reintegration of settled phytoplankton)

The net phytoplankton mass balance at diurnal scale of a day n was then given by the following sum:

$$V(C^{n+1} - C^n) = \quad (1 + P_G^{\max})[S(\bar{w}^+ - w_s)\tau_c^+ + S(\bar{w}^- - w_s)\tau_c^-]C^n - Sw_s(\tau_{day} - \tau_c)C^n.$$

We defined $\Delta C_n^{n+1} \equiv C^{n+1} - C^n$. We then expressed the rate of chance of concentration by replacing the above defined quantities in terms of the convective scales and the β and γ parameters, which set the aspect ratio between the mean upward velocity and the mean downward velocity:

$$\frac{\Delta C_n^{n+1}}{C^n} = (1 + P_G^{max})\frac{S}{V}(\gamma\bar{w}_* - w_s)\frac{\beta}{\beta+\gamma}\tau_c - \frac{S}{V}(\beta\bar{w}_* + w_s)\frac{\gamma}{\beta+\gamma}\tau_c - \frac{S}{V}w_s(\tau_{day} - \tau_c),$$

$$\frac{\Delta C_n^{n+1}}{C^n} = -\frac{S}{V}w_s\tau_c + P_G^{max}\frac{S}{V}(\gamma\bar{w}_* - w_s)\frac{\beta}{\beta+\gamma}\tau_c - w_s\frac{S}{V}(\tau_{day} - \tau_c)\frac{\Delta C_n^{n+1}}{C^n} = P_G^{\max}\frac{S}{V}(\gamma\bar{w}_* - w_s)\frac{\beta}{\beta+\gamma}\tau_c - w_s\frac{S}{V}\tau_{day}$$

.

To have a (positive) growth rate in time, then

$$\frac{\Delta C_n^{n+1}}{C^n} > 0,$$

which is satisfied by the following inequality:

$$\left[P_G^{\max}(\gamma\bar{w}_* - w_s)\frac{\beta}{\beta+\gamma}\tau_c - w_s\tau_{day}\right] > 0.$$

For a general case, with symmetrical distribution between upward and downward convective plumes, $\beta \sim 1$ and $\gamma \sim 1$:

$$\left[P_G^{\max}(\bar{w}_* - w_s)\frac{1}{2}\tau_c - w_s\tau_{day}\right] > 0.$$